Check for updates

View Article Online
View Journal

Nanoscale

Accepted Manuscript

This article can be cited before page numbers have been issued, to do this please use: I. G. G. ZIZZARI, V. Gigli, T. Gentili, C. Tortolini, A. Latini, A. Rughetti, M. C. di Gregorio, A. Isidori, M. Nuti and R. Antiochia, *Nanoscale*, 2025, DOI: 10.1039/D5NR00471C.

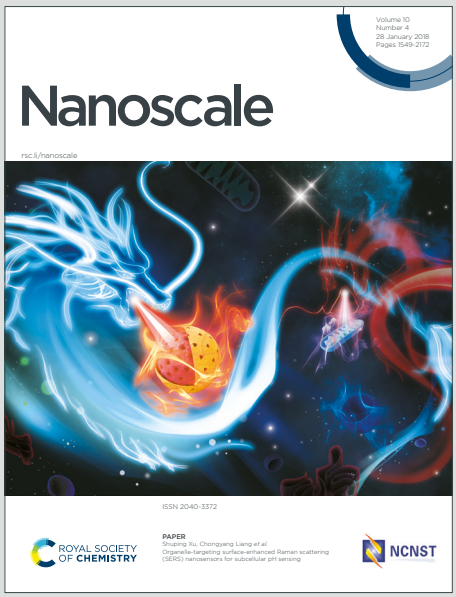

This is an Accepted Manuscript, which has been through the Royal Society of Chemistry peer review process and has been accepted for publication.

Accepted Manuscripts are published online shortly after acceptance, before technical editing, formatting and proof reading. Using this free service, authors can make their results available to the community, in citable form, before we publish the edited article. We will replace this Accepted Manuscript with the edited and formatted Advance Article as soon as it is available.

You can find more information about Accepted Manuscripts in the Information for Authors.

Please note that technical editing may introduce minor changes to the text and/or graphics, which may alter content. The journal's standard Terms & Conditions and the Ethical guidelines still apply. In no event shall the Royal Society of Chemistry be held responsible for any errors or omissions in this Accepted Manuscript or any consequences arising from the use of any information it contains.

ROYAL SOCIETY OF CHEMISTRY

rsc.li/nanoscale

Please do not adjust margins

View Article Online
DOI: 10.1039/D5NR00471C

ARTICLE

An ecofriendly iron MOF-based immunosensor for sensitive detection of vascular endothelium growth factor in serum of cancer patients

Received 00th January 20xx,
Accepted 00th January 20xx

DOI: 10.1039/x0xx00000x

Ilaria Grazia Zizzari[a], Valeria Gigli[a], Tommaso Gentili[b], Cristina Tortolini[a], Alessandro Latini[b], Aurelia Rughetti[a], Maria Chiara di Gregorio[b], Andrea Isidori[a], Marianna Nuti[a], Riccarda Antiochia[c†]

This work demonstrates the potential of an iron-based metal-organic framework, MIL-100(Fe), to effectively modify a multi-wall carbon nanotubes (MWCNTs) screen printed electrode (SPE) for enhanced electrochemical immunosensing of the vascular endothelium growth factor (VEGF), which has been recently considered a promising tumor biomarker. MIL-100(Fe) has been synthetized according to an ecofriendly, sustainable, heatless water-based technique at various synthesis reaction times. The morphological, structural and electrochemical properties of the different samples of MIL-100(Fe) were evaluated using several physical and electrochemical techniques. The MIL-100(Fe) after 48 h owned a crystalline microporous-mesoporous structure, with superior properties, that is larger BET surface area of 1082 ± 18 m^2/g, larger pore volume of 0.696 cm^3/g and better electroconductivity. After optimizing the experimental conditions, the MIL-100(Fe)48h/MWCNTs/SPE based immunosensor showed a linear range between 100 and 480 pg mL^{-1}, a LOD of 50 pg mL^{-1} (3s/S), a sensitivity of 0.017 mA mL pg^{-1}, good reproducibility and high selectivity. In addition, the developed immunosensor was applied to satisfactorily detect VEGF in human serum samples of cancer patients, compared to traditional ELISA method. Considering the sustainable and easy fabrication of the proposed platform, it may provide promising application as a point-of-care (PoC) device for VEGF detection for early-stage diagnosis of cancer patients.

Keywords: *metal organic framework; MIL-100(Fe); immunosensor; VEGF; cancer diagnosis.*

Open Access Article. Published on 28 February 2025. Downloaded on 3/7/2025 11:32:11 AM.
This article is licensed under a Creative Commons Attribution-NonCommercial 3.0 Unported Licence.

Nanoscale Accepted Manuscript

Introduction

Metal-organic frameworks (MOFs) are an emerging class of crystalline porous nanomaterials that consist of metal ions or clusters linked by organic ligands to form a 3D molecular framework[1-3].

In recent years, more than 20,000 MOFs have been described[4]; moreover, they can be combined with other compounds to create composite-MOFs with unique characteristics[5-9] for potential applications in gas adsorption[10-14], catalysis[15-18], energy storage[19-21], biomedicine[22,23] and (bio)sensing[24-28]. In particular, their promising properties for application in sensors and biosensors field are their high surface area, high and tunable porosity and the possibility of an easy functionalization pre-, post- and during the synthesis, leading to virtually an infinite number of biomolecules and/or electroactive molecules[29-33].

[a] *Department of Experimental Medicine, Sapienza University of Rome, Italy*
[b] *Department of Chemistry, Sapienza University of Rome, Italy*
[c] *Department of Chemistry and Drug Technologies, Sapienza University of Rome, Italy*
†Corresponding author: Prof. Riccarda Antiochia, riccarda.antiochia@uniroma1.it

Supplementary Information available: [details of any supplementary information available should be included here]

Please do not adjust margins

View Article Online
DOI: 10.1039/D5NR00471C

Open Access Article. Published on 28 February 2025. Downloaded on 3/7/2025 11:32:11 AM.
This article is licensed under a Creative Commons Attribution-NonCommercial 3.0 Unported Licence.

However, some important drawbacks should be mentioned, in particular their poor conductivity because of the insulating nature of the organic-ligands and the participation of the metal-ions D-orbitals in coordination bonds, which do not allow an efficient delocalization of electrons across the framework. In order to overcome these issues, MOFs have been combined with different nanomaterials in the construction of the electrochemical platforms, such as graphene, carbon nanotubes (CNTs) and metallic nanoparticles (NPs).

CNTs have been largely utilized in electrochemical biosensors development thanks to their excellent electrical conductivity, high surface area and high mechanical strength, which can enhance the electron transfer and stability of modified electrodes[34].

Among the different types of MOFs, Fe-based MOFs have recently attracted special interest in biosensing applications in the biomedical field, for their low toxicity and high thermal/chemical stability. On the other hand, iron is environmentally friendly, compared to other metals, inexpensive and exhibits an interesting redox behavior of the Fe(II)-Fe(III) redox sites[35].

Moreover, Fe-MOFs, especially the MIL series, are not only structurally flexible, but also have good water solubility, which make them a promising material for sensing applications[36].

The most popular Fe-based MOF is MIL-100(Fe), prepared by a combination of trimesic acid, as organic linker, and Fe(II) salt[37,38]. This is among the most used MOF in biomedicine and drug delivery, due to its high stability in various physiological conditions, low toxicity and environment compatibility. It is actually one of the highest porous MOFs available that can be produced by a large-scale hydrothermal synthesis[38]. The hierarchically mesoporous crystalline 3D Fe(III) trimesate has two sets of mesoporous cages with different diameters (24 Å and 29 Å) that are accessible through microporous windows (ca. 8.6 Å and ca. 4.7-5.5 Å)[39-42].

At present, the biggest challenge in the MIL-100(Fe) synthesis is to yield a highly crystalline MOF under mild conditions, avoiding the use of toxic reagents, HF (hydrofluoric acid), high temperature and pressure. The most conventional synthesis of MIL-100(Fe) is carried out at 150 °C for 6 days in the presence of the environmentally harmful and corrosive acids HF and HNO_3, and the recovered solid should be washed at 80 °C in water for 3h[34]. Successively, some works reported milder synthesis approaches, avoiding the use of corrosive acids and/or using lower temperatures[41,43]. Guesh et al. reported the synthesis of MIL-100(Fe) at room temperature in water in a few hours without any corrosive inorganic acid[44,45].

In this work, a sustainable water-based heatless synthesis method of MIL-100(Fe) was developed, and the resulting MOF was utilized for the modification of a MWCNTs/SPE for the construction of a novel electrochemical platform for VEGF detection. To understand the electrocatalytic properties of the newly synthetized MOF, it is necessary to know and control the synthetic parameters in order to make structure-property relationships. In our study, we extracted from the synthesis mixtures materials at different synthesis times and investigated their structure and electrochemical properties using several techniques. The platform which showed the best electrochemical performances was utilized for the construction of a voltametric immunosensor for the detection of VEGF in human serum samples. VEGF is an important cancer biomarker[46,47], increased in various hypoxic tumors, including ovarian, breast and kidney cancers[48,49]. It represents the most potent inducer of neo-angiogenesis in cancer, able to promote tumor growth and metastasis.

Nanoscale Accepted Manuscript

 This journal is © The Royal Society of Chemistry 20xx

Please do not adjust margins

View Article Online
DOI: 10.1039/D5NR00471C

Open Access Article. Published on 28 February 2025. Downloaded on 3/7/2025 11:32:11 AM.
This article is licensed under a Creative Commons Attribution-NonCommercial 3.0 Unported Licence.

Nanoscale Accepted Manuscript

Moreover, high levels of VEGF have been correlated with poor clinical outcomes in several tumors[50-52], also in early-stage diagnosis of cancer patients. Schluter A. et al. suggested in fact that high levels of VEGF might help to identify patients with poor prognoses in early-stage of laryngeal squamous cell carcinoma, improving the clinical management of these patients[53]. In addition to angiogenic effects, VEGF modulates the immune system, blocking the anti-tumor immune response[54]. Indeed, VEGF reduces the number of T lymphocyte precursors in the thymus and the number of differentiated T cells in the lymphoid organs and attenuates their effector function. In addition, VEGF promotes immunosuppression in the tumor microenvironment by accumulating regulatory T cells and favoring to T cell exhaustion. Therefore, VEGF contributes in the early stage of tumor development, during progression and metastasis. ~~Therefore,~~ Thus, VEGF has become the major target in most anti-angiogenic cancer therapies, in monotherapy or combination with immunotherapy. VEGF inhibition normalizes tumor vasculature, reducing vascular permeability and improving the delivery of oxygen, immune cells and drugs to tumor site. Consequently, the detection of VEGF levels in clinical samples of cancer patients with an ecofriendly, fast, cheap and portable device is of extreme importance for diagnosis, prognosis, and therapeutic monitoring of various types of cancer, also in early stage.

Experimental results and Discussion

Structural and morphological characterization of MIL(100)-Fe

The MIL-100 used in this work was synthesized by a "green" synthesis reported by Guesh et al.[44], which involves room temperature and water reaction conditions[38,55,56], with a synthesis time of 24h. In the synthesis a water solution of $FeCl_2$ is dropped in a basified solution of the organic linker trimesic acid and allowed to stir at room temperature up to the formation of a reddish powder. These conditions enable the change of the Fe oxidation state from 2^+ to 3^+ and concurrently the formation of the coordinative metal-organic network. In order to investigate the effect of the different synthesis times on both crystallinity and electrochemical performances of MIL-100, three different stirring times were tested, namely 2h, 24h and 48 hours. The MIL-100(Fe) formation and the purity of its crystal phase was primarily checked by powder X-ray diffraction (PXRD). PXRD unambiguously proved that the MIL-100 synthesis was accomplished for the samples reacted for 24 and 48 h: the comparison of the experimental PXRD patterns and the analogue spectrum generated from the literature reported single crystal data[38], shows consistency both in terms of peaks' number and position (Figure 1). The PXRD peaks are particularly sharp, intense and defined for the sample at 48 h, indicating a good degree of crystallinity.

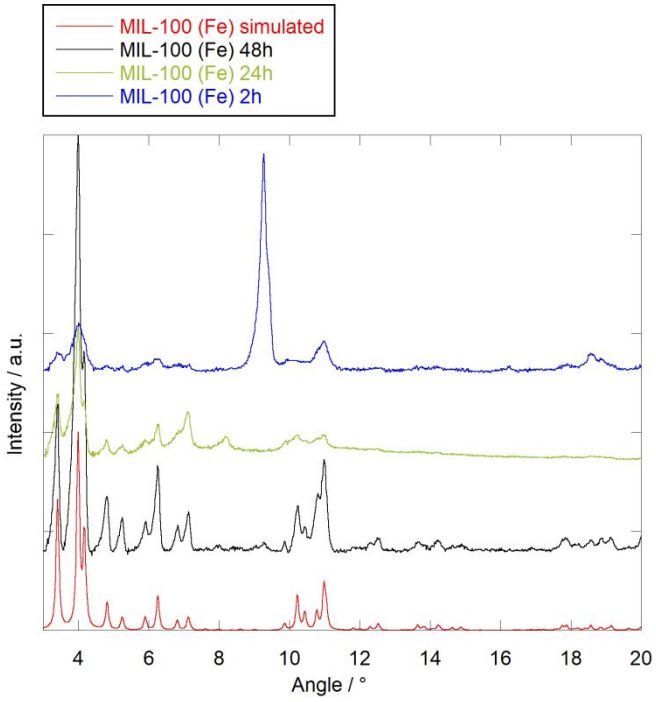

Please do not adjust margins

View Article Online
DOI: 10.1039/D5NR00471C

Figure 1. PXRD patterns of MIL-100(Fe) at 2h (blue curve), 24 h (green curve), 48 h (black curve) of synthesis. The red curve is the simulated MIL-100(Fe) spectrum that is generated from the Single Crystal X-ray Diffraction cif file. (ref. 38).

Raman spectroscopy was also used as tool to confirm the synthesis of 48 h MIL-100 (Figure 2).

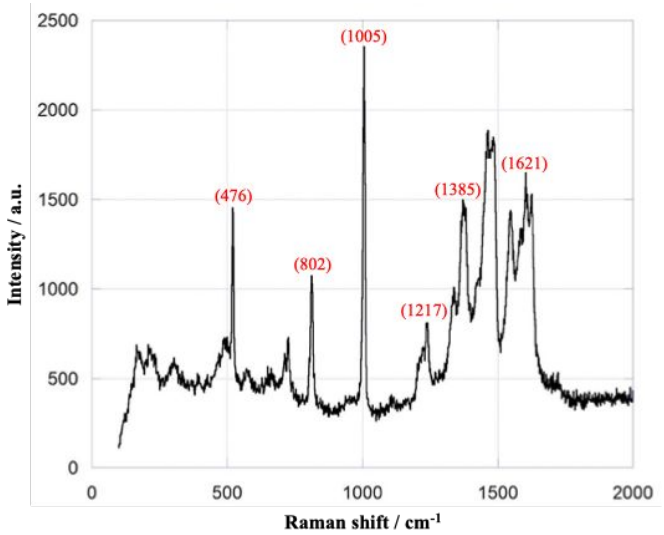

Figure 2. Raman spectrum of 48 h MIL-100(Fe).

Indeed, the profiles of the Raman spectrum perfectly matches the one reported in the literature for MIL-100[56]: peaks at 800 cm^{-1} and 1000 cm^{-1} are characteristic of the trimesate linker, the peak around 1200 cm^{-1} is related to the C–O–Fe stretching of the coordination nodes whereas bands in the 1400 cm^{-1} - 1600 cm^{-1} range corresponds to the H–O–H bonding vibrations, demonstrating the presence of coordinated water molecules in the framework. Moreover, XPS measurements were run on the pristine 48 h MIL-100(Fe) sample in order to ascertain its chemical composition. The results, reported in Figure 3, show that the Fe 2p ionization signal (Figure 3 a) is split due to spin-orbit coupling (j = 3/2 and ½), with the j = 3/2 component falling around 712 eV binding energy (BE), which is compatible with the presence of Fe^{3+}. The C 1s region (Figure 3 b) is associated to the carbon containing molecular species and shows the presence of both an aromatic C component (peaked at 285 eV BE) and a high BE is associated to carboxyl groups (289 eV BE).

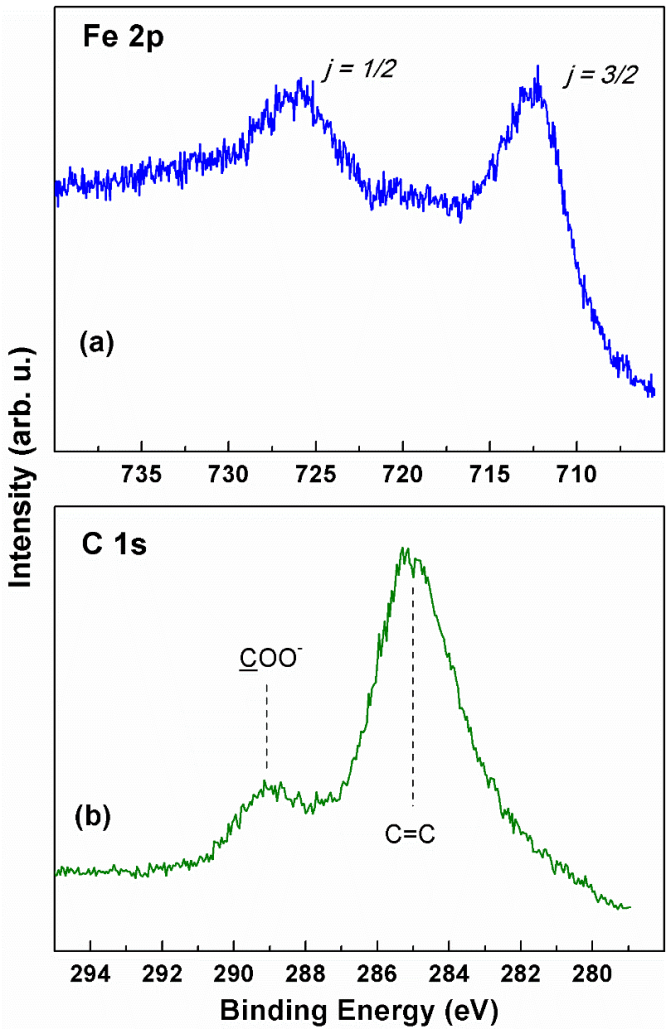

Figure 3. XPS spectra of 48 h MIL-(100)Fe in the ionization regions of (A) C 1s and (B) Fe 2p.

These findings are fully compatible with the expected composition of MIL-(100)Fe. Thermostability analysis have been also conducted by TGA/DTA measurements

Open Access Article. Published on 28 February 2025. Downloaded on 3/7/2025 11:32:11 AM.
This article is licensed under a Creative Commons Attribution-NonCommercial 3.0 Unported Licence.

Nanoscale Accepted Manuscript

This journal is © The Royal Society of Chemistry 20xx

View Article Online
DOI: 10.1039/D5NR00471C

and totally agrees with analogues data reported in the literature (Figure 4)[58].

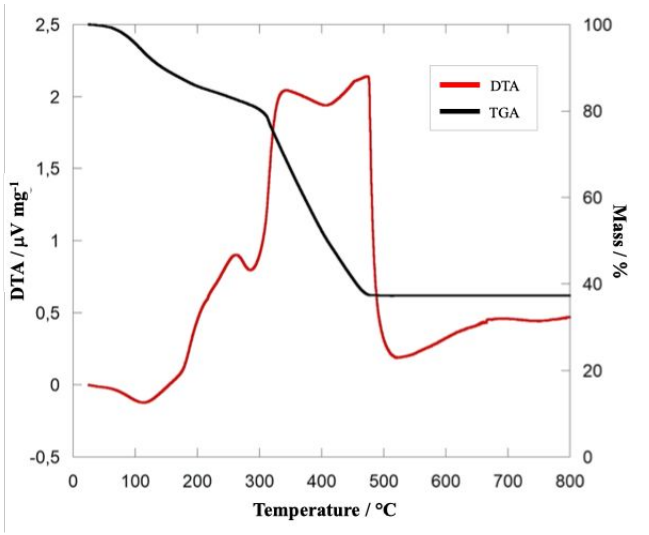

Figure 4. TG/DTA curves of 48 h MIL-100(Fe).

As reported in the TEM and SEM microscopy images, the MOFs after 24h and 48h appear as faceted and dipyramid structures (Figure 5 B and C, Figure 6 B and A). The average size of the crystals, measured as distance between the apexes of the dipyramids, is 168 ± 65 nm. EDS spectrum reports all the emission lines expected for the MIL-100(Fe) composition, namely C, O, Fe. Na presence is also highlighted; it is due from the NaOH use in the basification of linker solution (Figure 6). Performing a shorter time reaction (2 h) leads to a crystalline precipitate that does not match the PXRD profile of MIL-100(Fe): some of the MIL-100(Fe) peaks are just barely hinted (e.g. peaks at 3.4°, 4.0°, 6.3° and 11.0°) and a dominant and sharp peak is present at 9.3° 2θ. This latter peak can indicate a different phase, likely a kinetically stable phase that in prolonged reaction dissolves in favor of the thermodynamically stable MIL-100(Fe) crystal structure (Figure 1, blue curve). Although such PXRD peak has been observed in other reported studies44, in our case it appears much more intense. TEM and SEM images on the sample after 2h of reaction exhibit both unshaped material and faceted crystals (Figure 5 A, Figure 6C) with an average diameter of 80 ± 10 nm, resulting much smaller than the structures observed in the well- formed MIL-100(Fe). EDS spectra are again coherent with the expected composition.

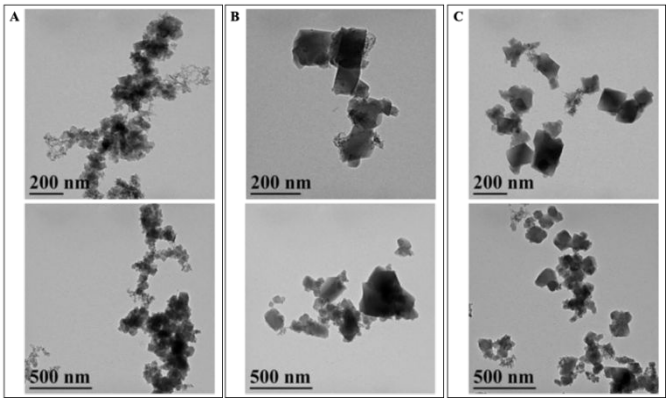

Figure 5. TEM images of MIL(100)-Fe after 2 h (A), 24h (B) and 48h (C) of synthesis.

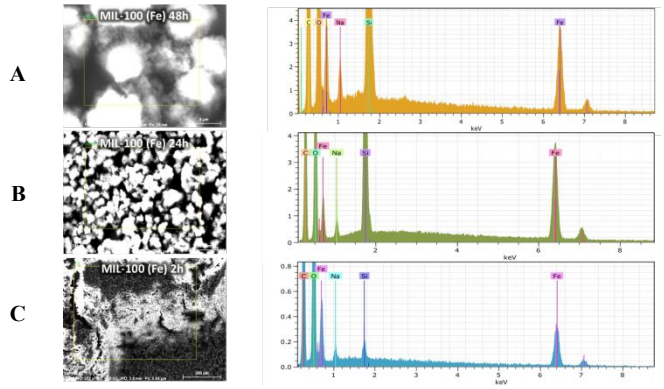

Figure 6. SEM-EDS spectra of MIL(100)-Fe after 48 h (A), 24h (B) and 2h (C) of synthesis.

To better investigate the effect of the different synthesis times, nitrogen adsorption isotherms of MIL(100)-Fe at 48h, 24h and 2h of reaction were performed and shown in Figure 7 (A,B and C). All N2-sorption curves indicate a combination of type I and IV isotherm according to IUPAC, typical of MIL-100(Fe), with a narrow hysteresis loop in the relative pressure (P/P0) range 0.8-1.0. The surface area was calculated using Brunauer-

Open Access Article. Published on 28 February 2025. Downloaded on 3/7/2025 11:32:11 AM.
This article is licensed under a Creative Commons Attribution-NonCommercial 3.0 Unported Licence.

Nanoscale Accepted Manuscript

View Article Online
DOI: 10.1039/D5NR00471C

Open Access Article. Published on 28 February 2025. Downloaded on 3/7/2025 11:32:11 AM.
This article is licensed under a Creative Commons Attribution-NonCommercial 3.0 Unported Licence.

Emmett-Teller model (BET) and the obtained values are reported in Table 1, together with the pore volume values. The pore size distribution (Figure 7 C) is consistent with the existence of the two types of mesopores and the corresponding microporous windows (Figure 7 D and E)[38,39]. Interestingly, it is seen that the MIL-100(Fe) at 48 h, which showed the higher crystallinity, has also the highest surface area (1082 ± 18 m2/g) and the highest pore volume (0.696 cm3/g), attesting a correlation between the crystallinity and the BET results. These values are slightly lower than those found in literature and similar to those reported by Ahmed et al.[59] for MIL-100(Fe), obtained by dry gel conversion from metallic iron without any acid and salt (Table S1).

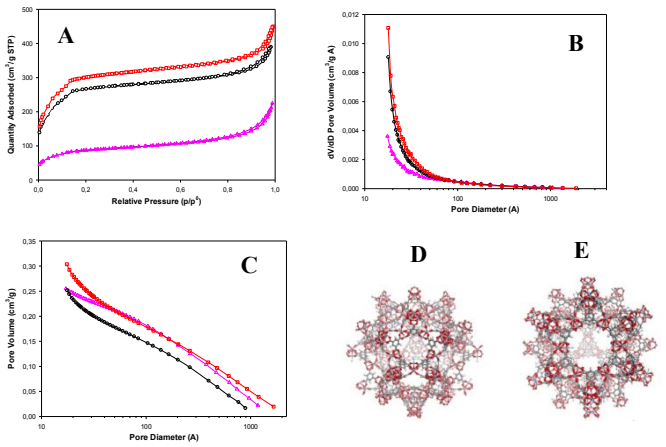

Figure 7. (A) BET nitrogen adsorption-desorption isotherms, (B) BHJ adsorption cumulative pore volumes, (C) BJH adsorption dV/dD pore volume of MIL-100(Fe) at 48 h (red curve), 24 h (black curve) and 2h (pink curve) of synthesis; MIL(100)-Fe mesoporous cages (D) medium cage (24 Å) and (E) large cage (29 Å) (ref. 38).

Electrochemical characterization of MIL-100(Fe)/MWCNTs/SPE

The electrochemical behavior of the MWCNT/SPE before and after the modification with MIL-100(Fe) was studied by CV experiments. Figure 8 shows the cyclic voltammograms obtained before (black curve) and after the modification of MWCNTs/SPE with MIL-100(Fe) at different synthesis times. In all CVs, a pair of quasi-reversible redox peaks is evident, with slight increases in the peak-to-peak separations (ΔE_p) observed with modified electrodes. The electroactive area (A_e) and roughness factor (ρ) were subsequently calculated from the CV curves and reported in Table 1. The A_e was determined by plotting the peak current against the square root of the scan rate ($v^{1/2}$) and incorporating the obtained slope value into the following Randles-Sevcik equation[60].

$$I_p = 2.686 \times 10^5 n^{\frac{3}{2}} A_e D_0^{\frac{1}{2}} C_0 v^{\frac{1}{2}} \quad (1)$$

where I_p represents the peak current (A), n the number of electrons involved, A_e the electroactive area (cm^2), D_0 the diffusion coefficient (7.6×10^{-6} cm^2 s^{-1} for ferricyanide), C_0 the concentration (mol cm^{-3}), and v the scan rate (V s^{-1}). The roughness factor (ρ) was assessed as the ratio of electroactive area to geometric area.

It is clear that by prolonging the synthesis time to 48 h there is a large increase of the peak current (blue curve) compared to 24 h (green curve) and 2 h (red curve). This large enhancement may be ascribed to the better redox conductivity of 48 h MIL(100)-Fe film drop-cast on the electrode surface, thanks to the higher surface area and higher porosity of its microporous-mesoporous structure, with a consequent increase of the electrode surface area[61]. Table 2 displays also the heterogeneous electron transfer rate constants (k_0, cm s^{-1}) for the MWCNTs/SPE before

Nanoscale Accepted Manuscript

This journal is © The Royal Society of Chemistry 20xx

Please do not adjust margins

View Article Online
DOI: 10.1039/D5NR00471C

Open Access Article. Published on 28 February 2025. Downloaded on 3/7/2025 11:32:11 AM.
This article is licensed under a Creative Commons Attribution-NonCommercial 3.0 Unported Licence.

and after the modification with MIL-100(Fe), calculated using the Lavagnini et al. method, which is an integration of Klingler–Kochi and Nicholson and Shain methods for irreversible and reversible systems, respectively[62]. The 48h MIL-100(Fe)/MWCNTs/SPE electrode exhibited the highest k_0 value, confirming that the higher crystallinity and higher porosity of the 48 h MOF facilitate a faster electron transfer kinetics. As shown, the optimum synthesis time resulted to be 48 h in terms of both crystallinity, porosity and electrochemical performances and therefore the 48 h MIL-100(Fe) was chosen for further experiments. The term MIL-100(Fe) will refer to 48 h MIL-100(Fe) in the followings.

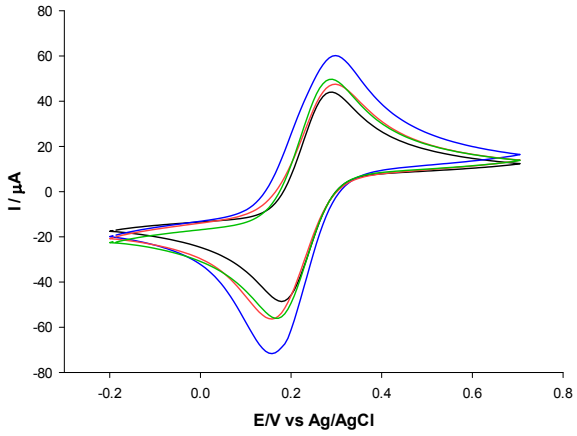

Figure 8. CV curves of a MWCNTs/SPE (black curve), MIL100(Fe)2h/MWCNTs/SPE (red curve), MIL100(Fe)24h/MWCNTs/SPE (green curve) and MIL100(Fe)48h/MWCNTs/SPE (blue curve) measured in 2.5 mM Zobell's solution. Scan rate: 25 mV/s.

Electrochemical characterization of the VEGF immunosensor platform

The electrochemical behavior of the MWCNTs-SPE electrode following each surface modification step conducted for the development of the VEGF immunosensor was investigated using differential pulse voltammetry (DPV) and electrochemical impedance spectroscopy (EIS).

DPV characterization Figure 9 A shows the DPV curves corresponding to each surface modification step of the VEGF immunosensor. Compared to unmodified MWCNTs/SPE (black curve), a significant increase of the peak current is registered after the modification with MIL-100(Fe) (blue curve), thanks to the large conductive properties of MOF. Then, a progressive decrease of the peak current is registered corresponding to the following steps: (i) anchoring of VEGF antibody (red curve); (ii) saturating with HSA (green curve); (iii) formation of VEGF Ab-Ag complex (orange curve). These results indicate that the electron transfer of the electrode is progressively hampered by the insulating nature of antibody, HSA and antigen biomolecules, thus confirming the successful immobilization of these biomolecules on the electrode surface.

EIS characterization

The Nyquist plots corresponding to each modification step of the immunosensor platform were recorded and fitted by the simple Randles circuit (Figure 9B). Compared to bare electrode (black curve), after the immobilization of MIL-100(Fe), it is possible to observe a slight decrease of the R_{CT} value (259 Ω), indicating a higher electron transfer rate between the redox probe and the electrochemical double layer, probably due to the formation of electrostatic interactions between MIL-100(Fe) and the -COOH functional groups of MWCNTs. This results in a smaller semicircle (blue curve), demonstrating that the MOF effectively enhances the conductivity of the electrode/electrolyte interface, thanks to its superior electroconductive properties. A significant increase in the semicircle diameter (R_{CT}) was observed following the immobilization of VEGF Ab (red curve), indicating a well-oriented affinity binding of the antibodies, leading to electron transfer hindrance.

Nanoscale Accepted Manuscript

Please do not adjust margins

View Article Online
DOI: 10.1039/D5NR00471C

Open Access Article. Published on 28 February 2025. Downloaded on 3/7/2025 11:32:11 AM.
This article is licensed under a Creative Commons Attribution-NonCommercial 3.0 Unported Licence.

Further R_{CT} increases were observed after the immobilization of HSA protein (green curve), used as blocking agent to prevent non-specific interactions, and VEGF antigen (orange curve). In all cases the R_{CT} increases are due to the mass-transfer limiting of $[Fe(CN)_6^{3-/4-}]$ to the electrode surface by the immobilized biomolecules. The acquired data were fitted using the Randles equivalent circuit [R(Q[RW])], incorporating components such as the electrolyte solution resistance (Rs), charge transfer resistance (R_{CT}), constant phase element (Q), and the Warburg element (W) (Figure 10, inset), and reported in Table 3. In particular, the R_{CT} value exhibited a 257%, 476%, and 644% enhancement after the immobilization of VEGF antibody, HSA protein, and VEGF antigen, respectively. This enhancement was calculated using the following equation:

$$\Delta R_{CT}\% = \frac{R_{CTmod} - R_{CTi}}{R_{CTi}} \times 100 \quad (2)$$

where R_{CTi} and R_{CTmod} are the charge transfer resistance for MIL-100(Fe)/MWCNTs/SPE before and after each surface modification step.

Optimization of the VEGF Electrochemical Platform

Various parameters such antibody concentration, its binding time and antigen incubation time were optimized by DPV experiments, in order to achieve the best electrochemical performances of the sensing platform. As shown in Figure S1, the current density reached a minimum value, attesting saturation of the electrode surface, at an antibody concentration of 10 μg mL^{-1} and with a binding time of 4 h. As for VEGF antigen incubation, different time periods between 10 and 90 minutes have been tested and an incubation time of 60 minutes resulted to be the optimum value showing a minimum current response.

(A)

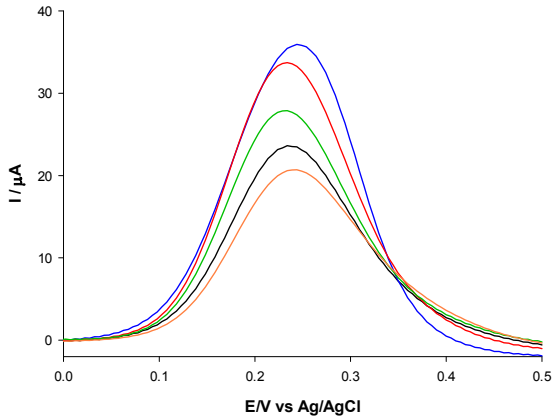

(B)

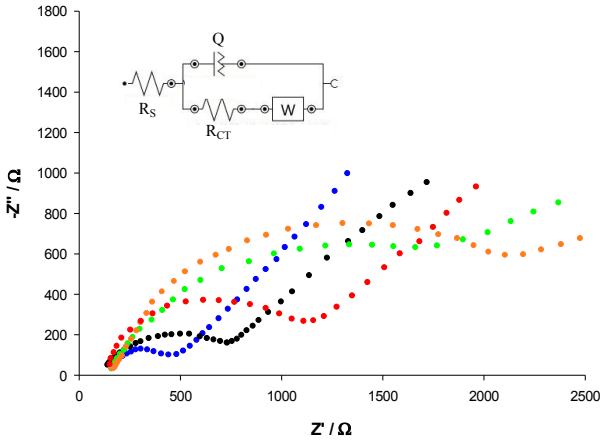

Figure 9. (A) DPV curves of a MWCNTs/SPE (black curve), MOF/MWCNTs/SPE (blue curve), Ab/MOF/MWCNTs/SPE (red curve), HSA/Ab/MOF/MWCNTs/SPE (green curve) and Ag/HSA/Ab/MOF/MWCNTs/SPE (orange curve) measured in 2.5 mM Zobell's solution; VEGF antibody = 10 μg mL^{-1}; [VEGF Ag] = 500 pg/mL; (B) Nyquist plots of: MWCNTs/SPE (black curve), MOF/MWCNTs/SPE (blue curve), Ab/MOF/MWCNTs/SPE (red curve), HSA/Ab/MOF/MWCNTs/SPE (green curve) and Ag/HSA/Ab/MOF/MWCNTs/SPE (pink curve) measured in 2.5 mM Zobell's solution. Inset: simple Randles circuit. [VEGF Ag] = 500 pg/mL

Nanoscale Accepted Manuscript

This journal is © The Royal Society of Chemistry 20xx

Please do not adjust margins

View Article Online
DOI: 10.1039/D5NR00471C

Open Access Article. Published on 28 February 2025. Downloaded on 3/7/2025 11:32:11 AM.
This article is licensed under a Creative Commons Attribution-NonCommercial 3.0 Unported Licence.

VEGF immunosensor

DPV experiments were performed in the development of the VEGF immunosensor. At increasing antigen concentrations, a progressive reduction of the oxidation current signal (Figure 10 A) is registered, due to the non-conductive nature of the antigen. The calibration curve, shown in Figure 10 B, demonstrates a dynamic linear relationship between current density and VEGF concentration in the range 100-480 pg mL^{-1}, a detection limit (LOD) of 50 pg mL^{-1}, calculated with the formula $3\sigma/S$, with σ the standard deviation of the intercept and S the slope of the calibration plot, and a sensitivity of 0.017 mA mL $pg^{-}1$. The corresponding linear regression equation resulted to be $y = 0.017x - 1.758$ with an R2 value of 0.994 (n=3, RSD < 5 %). Table 4 shows a brief overview of other VEGF voltammetric immunosensors reported in literature. Based on the reported data, there is only another cobalt-MOF based immunosensor for VEGF detection[63], but it shows 4 times higher LOD value compared to the Fe-MOF developed in our work. As for the dynamic linear range, the proposed immunosensor showed a more restricted linear range but it is within the physiological concentration of VEGF in human serum, considering a threshold limit among healthy individuals and cancer patients of about 210 pg/mL[64,70]. Moreover, the MIL-100(Fe) has been synthetized according to a heatless procedure, whereas the Co-based MOF has been synthesized according to the classical hydrothermal method, which requires the use of a thermal autoclave. Most other works reported in Table 4 have been tested in buffer and not in human/animal serum and therefore the results are not directly comparable. Lastly, the very recent nanoporous Au-based immunosensor[70], tested in human serum spiked with VEGF concentrations, showed a remarkable LOD and linear response range, but it must be considered that its preparation requires a silver and gold deposition step on a fluorine-doped tin oxide substrate, followed by a thermal annealing process in a furnace at 550 °C and a dealloying process with HNO_3 solution. The findings illustrate the superior characteristics of the proposed MIL-100(Fe) electrochemical platform, in terms of sustainability, environmental friendliness, and costs, as it does not require high temperature, high pressure or toxic chemicals.

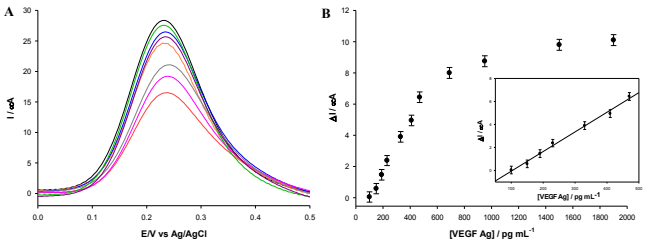

Figure 10. Panel A: DPV of HSA/Ab/MOF/MWCNTs/SPE (black curve) modified with varying concentration of VEGF Ag (from 150-1900 pg mL^{-1}; from green to red curve) measured in 2.5 mM Zobell's solution. Panel B: Calibration plot for different VEGF concentrations (from 150-1900 pg mL^{-1} in PBS pH 7.2). Inset: the magnification of linear range. Experimental conditions: 2.5 mM Zobell's solution; VEGF antibody = 10 mg mL^{-1}

Selectivity, reproducibility and stability of the VEGF immunosensor

The selectivity of the proposed platform was assessed by comparing the DPV signals obtained in presence of VEGF with those obtained in presence of other proteins, such as Bovine Serum Albumin (BSA), Prostate Specific Antigen (PSA), glucose (Glu), and cholesterol (Cho). The DPV signals were recorded after a 30 minute incubation period of each protein on the HSA/Ab/MIL-100(Fe)/MWCNTs/SPE platform. In particular, a concentration of 500 pg/mL was employed for the VEGF protein, while a concentration of 5000 pg/mL was utilized for the four interferents tested. No significant signals were detected for all interferents, despite their use at a ten times higher concentration (Figure 11), attesting

Nanoscale Accepted Manuscript

Please do not adjust margins

View Article Online
DOI: 10.1039/D5NR00471C

Open Access Article. Published on 28 February 2025. Downloaded on 3/7/2025 11:32:11 AM.
This article is licensed under a Creative Commons Attribution-NonCommercial 3.0 Unported Licence.

the high selectivity of the proposed immunosensor, thanks to the specificity of the properly oriented VEGF antibody recognition sites towards the VEGF target antigen. The reproducibility was evaluated by measuring 500 pg mL^{-1} VEGF with ten immunosensors fabricated under identical conditions. The relative standard deviation (RSD) was calculated to be 7.4%, indicating a satisfactory reproducibility. The stability of the VEGF platform was also evaluated by DPV analysis. The electrode was kept at 4°C for a period of 30 days, with regular monitoring every 5 days. During the first 10 days, the current remained quite stable and after day 10 the current started to gradually decline over time. However, the immunosensor maintained more than 85% of the current response after 1 month, indicating a very good storage stability, as illustrated in Figure S2.

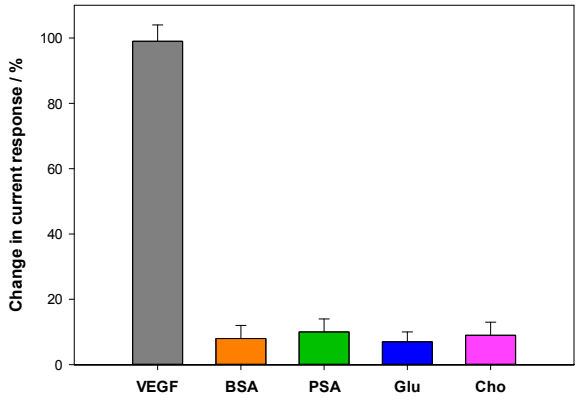

Figure 11. Histograms of selectivity assay for VEGF (500 pg/mL) vs.different potential interferents (5000 pg/mL) in 2.5 mM Zobell's solution.

Application in real serum samples

The proposed immunosensor was tested in 5 human serum samples of cancer patients. Table 5 shows the correlation between the outcomes of the developed immunosensor and the conventional ELISA method. Notably, the results exhibit a good agreement between the two techniques, with RSD% values ranging between 14 and 24. These results suggest the efficacy of the proposed immunosensor in accurately quantifying VEGF levels in human serum samples.

Materials and methods

Reagents

The anti-VEGF antibody (VEGF Ab) was purchased from Bio-Techne R&D Systems (Minneapolis, USA). The VEGF antigen (VEGF Ag) was purchased from Biorbyt (Cambridge, UK). Human Serum Albumin (HSA), potassium chloride (KCl, 99–100.5%), potassium ferricyanide (III) (K3[Fe(CN)6], 99.0%), potassium ferrocyanide (II) (K4[Fe(CN)6], 98.5–102.0%), sodium phosphate monobasic (NaH2PO4, ≥99%), sodium phosphate dibasic (Na2HPO4, ≥99%), iron(II) chloride tetrahydrate ($FeCl_2 \cdot 4H_2O$) and trimesic acid (H_3BTC) were purchased from Sigma Aldrich (Bucks, Germany). Each solution was made in phosphate buffer 0.1 M, KCl 0.1 M, and adjusted to a pH of 7.1 (PBS). During the investigations, high-purity deionized water sourced from Millipore (Molsheim, France) was employed (resistance: 18.2 MΩ cm at 25 ◦C; TOC < 10 µg L−1). All chemicals utilized were of analytical grade and were employed as received without undergoing any additional purification processes.

Electrochemical measurements and apparatus

Electrochemical measurements were conducted in a 10 mL conventional three-electrode thermostated glass cell (model 6.1415.150, Metrohm, Herisau, Switzerland), employing a multi-walled carbon nanotubes screen-printed electrode (MWCNTs-SPE, CNT110 Metrohm, Herisau, Switzerland), as working electrode, an external

Nanoscale Accepted Manuscript

 This journal is © The Royal Society of Chemistry 20xx

Please do not adjust margins

View Article Online
DOI: 10.1039/D5NR00471C

Open Access Article. Published on 28 February 2025. Downloaded on 3/7/2025 11:32:11 AM.
This article is licensed under a Creative Commons Attribution-NonCommercial 3.0 Unported Licence.

Ag/AgCl/KClsat electrode (198 mV vs. NHE), as reference electrode (cat. 6.0726.100, Metrohm, Herisau, Switzerland), and a glassy carbon rod, as counter electrode (cat. 6.1248.040, Metrohm, Herisau, Switzerland). The electrochemical measurements were performed using an Autolab Potentiostat/Galvanostat (Eco Chemie, The Netherlands).

Electrochemical impedance spectroscopy (EIS) data were obtained across the frequency range of 0.1–10^3 Hz, employing an AC signal with an amplitude of 10 mV and conducted under open-circuit potential (OCP) conditions.

Cyclic voltammetry (CV), Differential Pulse Voltammetry (DPV), and Electrochemical Impedance Spectroscopy (EIS) analyses were conducted utilizing a 15 mL solution comprising a mixture of 2.5 mM $Fe(CN)_6^{3-}/Fe(CN)_6^{4-}$ and 0.1 M KCl dissolved in distilled water, serving as the electrochemical redox probe (referred to as Zobell's solution).

The modification of all the functionalization steps were monitored by DPV and EIS experiments. The quantitative analysis for the construction of the immunosensor calibration curve was examined by a decrease in the peak current of DPV with the increase of the VEGF concentration.

In CV experiments, Zobell's solution was employed to ascertain the electroactive area (Ae), utilizing the Randles–Ševcik equation, the roughness factor ($\rho = A_e/A_{geom}$) and the heterogeneous electron transfer rate constant (k_0).

Scanning electron microscopy (SEM) and energy-dispersive X-ray spectroscopy (EDX)

SEM and EDX analyses were conducted using a High-Resolution Field Emission Scanning Electron Microscope (HR FESEM) Zeiss Auriga. Imaging was performed at an EHT voltage of 1.5/3 KV. For the sample preparation, 5µl of the sample was drop-casted on a silicon substrate and let it air dry.

Transmission electron microscopy (TEM)

TEM analysis was conducted using a JEOL 1200 EX2 instrument (JEOL USA, Massachusetts, USA) operating at an acceleration voltage of 150 kV. The size of the MOF-MIL 100(Fe) was assessed using ImageJ software25, analyzing a minimum of 10 TEM images. For TEM sample preparation, 10 µL of MOF-MIL 100 (Fe) solution was drop-cast onto a carbon film on mesh copper substrate (C200Cu, EMR Resolutions, Sheffield, UK) and allowed to air-dry for 24 hours.

Powder X-ray diffraction (PXRD)

PXRD patterns were obtained using a Malvern Panalytical X'Pert Pro diffractometer with Bragg-Brentano geometry, utilizing Cu Kα radiation with a wavelength of 0.154184 nm. The instrument was equipped with an ultrafast X'Celerator RTMS detector. The resulting scans were analyzed employing the X'Pert High Score Plus software.

X-ray photoelectron spectroscopy (XPS)

XPS measurements were carried out using a modified Omicron NanoTechnology MXPS system equipped with a monochromatic Al Kα (hν = 1486.7 eV) X-ray source. The C 1s and Fe 2p photoionization regions were acquired using an analyzer pass energy of 20 eV and take-off angle of 21° with respect to the sample surface normal.

Nanoscale Accepted Manuscript

Please do not adjust margins

View Article Online
DOI: 10.1039/D5NR00471C

Open Access Article. Published on 28 February 2025. Downloaded on 3/7/2025 11:32:11 AM.
This article is licensed under a Creative Commons Attribution-NonCommercial 3.0 Unported Licence.

Nanoscale Accepted Manuscript

Raman spectroscopy

Raman spectra were acquired at room temperature using backscattering geometry with an inVia Renishaw micro-Raman spectrometer. The spectrometer was outfitted with an air-cooled CCD detector and super-notch filters. An Ar^+ ion laser with a wavelength of 514 nm was employed, coupled to a Leica DLML microscope equipped with a 20x objective. Spectral resolution was set at 2 cm^{-1}, and spectra were calibrated using the 520.5 cm^{-1} line of a silicon wafer. Multiple spots on the sample surface were probed to acquire Raman spectra.

Thermogravimetry Differential Thermal Analysis (TG/DTA)

TG/DTA profiles were obtained by Netzsch STA 409 PC Luxx simultaneous thermal analyzer.

BET analysis

Surface area, Brunauer–Emmett–Teller (BET) multipoint method[71] and pore analysis were obtained by N_2 adsorption/desorption measurements, at the liquid nitrogen temperature (-196 °C), using a Micromeritics 3Flex 3500 analyzer. The samples were pre-treated under vacuum at 140°C for 4 hours. Pore size distribution was determined by the Barret–Joyner–Halenda (BJH) method[72]. The analysis of micropore was performed by the t-test[73]; total pore volume was determined by the rule of Gurvitsch[74].

Synthesis of MIL-100(Fe)

The MOF MIL-100(Fe) was synthesized following a procedure reported in the literature[44]. Two distinct solutions were prepared as follows: solution 1 comprised 167.1 mg of H_3BTC dissolved in 3 mL of an aqueous solution containing 1 M NaOH, while solution 2 was prepared by dissolving 226.6 mg of $FeCl_2 \cdot 4H_2O$ in 10.72 mL of distilled water. Subsequently, Solution 1 was cautiously added drop by drop into Solution 2 with continuous stirring. The stirring process persisted at room temperature for 24 hours or 48 hours. Following this, the resultant solution underwent three wash cycles with distilled water (10 mL each) and an additional wash with absolute ethanol (10 mL) via centrifugation at 6000 rpm. The resulting solid was then collected, resuspended in absolute ethanol, and designated as MOF-MIL 100 (Fe). An analogue reaction was also performed with a stirring time of 2 hours. A reddish crystalline precipitate forms but the crystalline phase does not match the one of MIL-100(Fe)

Immunosensor fabrication steps

The immunosensor was prepared according to the following steps: (1) 10 µL of MOF-MIL 100 (Fe) was deposited onto the working area of the MWCNTs-SPE via drop-casting and left to dry under vacuum for 2 hours; (2) the modified electrode was incubated in VEGF Ab solution (10 µg mL^{-1}, prepared in PBS 0.1 M, pH 7.1) for 4 hours; (3) 10 µL of HSA solution (0.25 % w/v) was dropped on the electrode surface (15 minutes), as a blocking agent to prevent non-specific interactions; (4) 10 µL of varying concentrations of VEGF Ag (ranging from 100 to 1900 pg mL^{-1}) were deposited onto the surface of the immunosensor and allowed to dry at room temperature for 30 minutes. The electrode surface was rinsed with a buffer solution at the conclusion of each fabrication step. The comprehensive modification stages of the working electrode for the construction of the VEGF immunosensor are delineated in Figure 12.

This journal is © The Royal Society of Chemistry 20xx

Please do not adjust margins

View Article Online
DOI: 10.1039/D5NR00471C

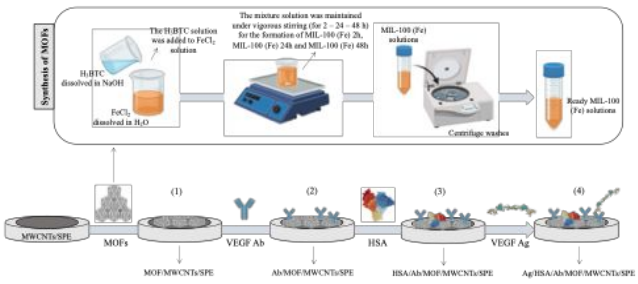

Figure 12. Preparation of modified MWCNTs/SPE by (1) MOF-MIL 100 (Fe) deposition, (2) VEGF Ab immobilization, (3) HSA surface blocking and (4) VEGF Ag bind. Inset: Procedure of MIL 100 (Fe) 2h, MIL 100 (Fe) 24h and MIL 100 (Fe) 48h synthesis.

Preparation of human serum sample

Sera were collected from metastatic renal cell carcinoma patients (from Policlinico Umberto I Hospital-Sapienza University of Rome) using BD Vacutainer Plus Plastic Serum tubes (Becton Dickinson) after centrifugation at 1,800 rpm for 10 minutes. Sera were then cryopreserved until use.

Before all measurements, human serum samples were appropriately diluted with 0.1 M pH 7.1 PBS (0.1 M KCl) at a dilution ratio of 1:100.

ELISA test

VEGF was evaluated in the serum of metastatic renal cell carcinoma patients before the beginning of therapy, using the Human VEGF Quantikine ELISA Kit, (R&D System, cat.no. DVE00) according to the manufacturer' instructions. The concentration of VEGF was evaluated by Multiskan FC (Thermo Fisher Scientific) at 450 nm of absorbance.

Conclusions

In summary, a novel ecofriendly immunosensor based on the immobilization of VEGF antibody on a MWCNTs/SPE modified with a MIL-100(Fe) has been constructed for the detection of VEGF tumor biomarker. The MIL-100(Fe) was successfully synthesized according to a "green" and sustainable method, which does not require any acid, harsh chemicals or heating. The morphology and structure, and, hence, the electrochemical properties of the so-synthesized MOF are directly correlated to its synthesis parameters. The synthesis reaction time has been varied in order to investigate this effect on the structure–electrochemical property relationships. To this end, the synthesis time has been varied in the range 2-48 h. Several physical measurements were conducted and the results obtained showed that the MIL-100(Fe) at 48 h showed the highest degree of crystallinity and the highest surface area and pore volume. The electrochemical experiments clearly attested a direct correlation between crystallinity, porosity and better electroconductive properties. The MIL-100(Fe)48h/MWCNTs/SPE based immunosensor showed a low detection limit of 50 pg mL^{-1} and a linear range in the clinically relevant range of VEGF in human serum, useful to help diagnosis, prognosis, and monitoring of several cancers associated with the expression of VEGF.

Since VEGF is recognized as an important cancer biomarker that plays a crucial role in the tumor growth, monitoring VEGF levels could allow the assessment of tumor status in many cases.

Hence, the proposed device is a beneficial immunosensor, which combines, unlike other VEGF immunosensors recently reported in literature, a sustainable, eco-friendly, easy and low-cost fabrication, with high sensitivity, good reproducibility, high selectivity, and an ideal dynamic range to detect VEGF in serum of cancer patients. Moreover, these characteristics highlight the appropriateness of the

Open Access Article. Published on 28 February 2025. Downloaded on 3/7/2025 11:32:11 AM.
This article is licensed under a Creative Commons Attribution-NonCommercial 3.0 Unported Licence.

Nanoscale Accepted Manuscript

Please do not adjust margins

proposed biosensor for extensive applications, positioning it as an optimal candidate in other research contexts and disease settings, such as infectious diseases.

Author contributions

I.G.Z and R.A: Conceptualization, data curation, investigation, funding acquisition, writing – original draft. V.G.: Investigation and data curation. T.G.: Investigation. C.T.: Investigation. A. L.: Investigation. A.R., A.I., M.N: Validation; R.A: Project administration, supervision. All authors: Writing – review & editing.

Conflicts of interest

There are no conflicts to declare.

Ethics Declarations

The study was conducted in accordance with the Declaration of Helsinki and with good clinical practice guidelines. All patients signed informed consent. The Institutional Ethics Committee of the involved institution (Policlinico Umberto I Hospital- Sapienza University Ethics Committee) agreed to the final version of the protocol (RIF.CE: 4181). All experiments were performed in accordance with relevant guidelines and regulations.

Data availability

The data supporting this article have been included as part of the Supplementary Information

Acknowledgements

The authors thank Prof. Andrea Marrani from Sapienza University for the support on the XPS and Raman analysis. Prof. Ida Pettiti is acknowledged for gas absorption measurements and BET analysis. Also, the assistance of Dr. Fabio Scirocchi from Sapienza University on ELISA measurements is gratefully acknowledged. Moreover, M. C. di G. acknowledges the support from the program ‘‘Rita Levi Montalcini for young researchers” of the Italian Ministry of University and Research.

Notes and references

1 M. Ding, R. W. Flaig, H.-L. Jiang and O. M. Yaghi, Chem Soc Rev, 2019, 48, 2783–2828.

2 S. Yuan, L. Feng, K. Wang, J. Pang, M. Bosch, C. Lollar, Y. Sun, J. Qin, X. Yang, P. Zhang, Q. Wang, L. Zou, Y. Zhang, L. Zhang, Y. Fang, J. Li and H. Zhou, Advanced Materials, DOI:10.1002/adma.201704303.

3 L. Chen, R. Luque and Y. Li, Chem Soc Rev, 2017, 46, 4614–4630.

4 M. Safaei, M. M. Foroughi, N. Ebrahimpoor, S. Jahani, A. Omidi and M. Khatami, TrAC Trends in Analytical Chemistry, 2019, 118, 401–425.

5 B. Le Ouay, C. Watanabe, S. Mochizuki, M. Takayanagi, M. Nagaoka, T. Kitao and T. Uemura, Nat Commun, 2018, 9, 3635.

6 G. Gao, Y. Wang, H. Zhu, Y. Chen, R. Yang, C. Jiang, H. Ma and Y. Lan, Advanced Science, DOI:10.1002/advs.202002190.

7 J. Lyu, X. Zhang, K. Otake, X. Wang, P. Li, Z. Li, Z. Chen, Y. Zhang, M. C. Wasson, Y. Yang, P. Bai, X. Guo, T. Islamoglu and O. K. Farha, Chem Sci, 2019, 10, 1186–1192.

8 X. Xie, X. Huang, W. Lin, Y. Chen, X. Lang, Y. Wang, L. Gao, H. Zhu and J. Chen, ACS Omega, 2020, 5, 13595–13600.

9 Q. He, P. Tu and J. L. Sessler, Chem, 2018, 4, 46–93.

10 C. Doonan, R. Riccò, K. Liang, D. Bradshaw and P. Falcaro, Acc Chem Res, 2017, 50, 1423–1432.

11 J. D. Evans, C. J. Sumby and C. J. Doonan, Chem. Soc. Rev., 2014, 43, 5933–5951.

12 E. Binaeian, E.-S. M. El-Sayed, M. Khanpour Matikolaei and D. Yuan, Coord Chem Rev, 2021, 430, 213738.

13 S. Ma, C. Wei, Y. Bao, Y. Liu, H. Jiang, W. Tong, D. Chen and X. Huang, Microchimica Acta, 2024, 191, 107.

14 R. E. Morris and P. S. Wheatley, Angewandte Chemie International Edition, 2008, 47, 4966–4981.

15 J. Lee, O. K. Farha, J. Roberts, K. A. Scheidt, S. T. Nguyen and J. T. Hupp, Chem Soc Rev, 2009, 38, 1450.

16 S. Subudhi, S. P. Tripathy and K. Parida, Catal Sci Technol, 2021, 11, 392–415.

17 H. Wang, B. Chen and D. Liu, Advanced Materials, DOI:10.1002/adma.202008023.

18 Q. Zhuang, R. Gao, M. Shi, X. Lin, A. Xie and W. Dong, ACS Appl Nano Mater, 2021, 4, 3869–3876.

19 M. Zhong, L. Kong, K. Zhao, Y. Zhang, N. Li and X. Bu, Advanced Science, DOI:10.1002/advs.202001980.

20 C. Hou and Q. Xu, Adv Energy Mater, DOI:10.1002/aenm.201801307.

21 Z. Liang, C. Qu, W. Guo, R. Zou and Q. Xu, Advanced Materials, DOI:10.1002/adma.201702891.

22 J. Yang and Y. Yang, Small, DOI:10.1002/smll.201906846.

23 X. Peng, L. Xu, M. Zeng and H. Dang, Int J Nanomedicine, 2023, Volume 18, 4907–4931.

24 J.-H. Li, Y.-S. Wang, Y.-C. Chen and C.-W. Kung, Applied Sciences, 2019, 9, 2427.

25 A. Morozan and F. Jaouen, Energy Environ Sci, 2012, 5, 9269.

26 L. E. Kreno, K. Leong, O. K. Farha, M. Allendorf, R. P. Van Duyne and J. T. Hupp, Chem Rev, 2012, 112, 1105–1125.

27 S.-N. Zhao, G. Wang, D. Poelman and P. Voort, Materials, 2018, 11, 572.

28 I. Stassen, N. Burtch, A. Talin, P. Falcaro, M. Allendorf and R. Ameloot, Chem Soc Rev, 2017, 46, 3185–3241.

29 L. Liu, Y. Zhou, S. Liu and M. Xu, ChemElectroChem, 2018, 5, 6–19.

30 G. Ashraf, T. Ahmad, M. Z. Ahmed, Murtaza and Y. Rasmi, Curr Top Med Chem, 2022, 22, 2222–2240.

31 S. Carrasco, Biosensors (Basel), 2018, 8, 92.

32 B. Mohan, S. Kumar, H. Xi, S. Ma, Z. Tao, T. Xing, H. You, Y. Zhang and P. Ren, Biosens Bioelectron, 2022, 197, 113738.

33 M. Daniel, G. Mathew, M. Anpo and B. Neppolian, Coord Chem Rev, 2022, 468, 214627.

34 Y. Song, Y. Shen, C. Gong, J. Chen, M. Xu, L. Wang and L. Wang, ChemElectroChem, 2017, 4, 1457–1462.

35 J. J. Delgado-Marín, J. Narciso and E. V. Ramos-Fernández, Materials, 2022, 15, 6499.

View Article Online DOI: 10.1039/D5NR00871C

Open Access Article. Published on 28 February 2025. Downloaded on 3/7/2025 11:32:11 AM. This article is licensed under a Creative Commons Attribution-NonCommercial 3.0 Unported Licence.

Nanoscale Accepted Manuscript

View Article Online
DOI: 10.1039/D5NR00471C

36 Q. Xia, H. Wang, B. Huang, X. Yuan, J. Zhang, J. Zhang, L. Jiang, T. Xiong and G. Zeng, Small, DOI:10.1002/smll.201803088.
37 Y. Fang, Z. Yang, H. Li and X. Liu, Environmental Science and Pollution Research, 2020, 27, 4703–4724.
38 P. Horcajada, S. Surblé, C. Serre, D.-Y. Hong, Y.-K. Seo, J.-S. Chang, J.-M. Grenèche, I. Margiolaki and G. Férey, Chem. Commun., 2007, 2820–2822.
39 A. García Márquez, A. Demessence, A. E. Platero-Prats, D. Heurtaux, P. Horcajada, C. Serre, J. Chang, G. Férey, V. A. de la Peña-O'Shea, C. Boissière, D. Grosso and C. Sanchez, Eur J Inorg Chem, 2012, 2012, 5165–5174.
40 F. Jeremias, A. Khutia, S. K. Henninger and C. Janiak, J. Mater. Chem., 2012, 22, 10148–10151.
41 F. Zhang, J. Shi, Y. Jin, Y. Fu, Y. Zhong and W. Zhu, Chemical Engineering Journal, 2015, 259, 183–190.
42 I. Bezverkhyy, G. Weber and J.-P. Bellat, Microporous and Mesoporous Materials, 2016, 219, 117–124.
43 F. Zhang, Y. Jin, J. Shi, Y. Zhong, W. Zhu and M. S. El-Shall, Chemical Engineering Journal, 2015, 269, 236–244.
44 K. Guesh, C. A. D. Caiuby, Á. Mayoral, M. Díaz-García, I. Díaz and M. Sanchez-Sanchez, Cryst Growth Des, 2017, 17, 1806–1813.
45 R. Zhu, M. Cai, T. Fu, D. Yin, H. Peng, S. Liao, Y. Du, J. Kong, J. Ni and X. Yin, Pharmaceutics, 2023, 15, 1599.
46 H. L. Goel and A. M. Mercurio, Nat Rev Cancer, 2013, 13, 871–882.
47 X. Guo, H. Yi, T. C. Li, Y. Wang, H. Wang and X. Chen, Biomolecules, 2021, 11, 253.
48 D. Pan, X. Gong, X. Wang and M. Li, Front Pharmacol, DOI:10.3389/fphar.2020.594050.
49 D. Klein, Front Oncol, DOI:10.3389/fonc.2018.00367.
50 T. C. Elebiyo, D. Rotimi, I. O. Evbuomwan, R. F. Maimako, M. Iyobhebhe, O. A. Ojo, O. M. Oluba and O. S. Adeyemi, Cancer Treat Res Commun, 2022, 32, 100620.
51 C. Zhang, L. Wang, C. Xiong, R. Zhao, H. Liang and X. Luo, J Orthop Surg Res, 2021, 16, 738.
52 O. G. Trifanescu, L. N. Gales, B. C. Tanase, S. A. Marinescu, R. A. Trifanescu, I. M. Gruia, M. A. Paun, L. Rebegea, R. Mitrica, L. Serbanescu and R. M. Anghel, Diagnostics, 2023, 13, 166.
53 Schlüter, P. Weller, O. Kanaan, I. Nel, L. Heusgen, B. Höing, P. Haßkamp, S. Zander, M. Mandapathil, N.Dominas, J. Arnolds, B. A Stuck, S. Lang, A. Bankfalvi, S. Brandau. 2018, 18, 272
54 J. M. Kim and D. S. Chen, Annals of Oncology, 2016, 27, 1492–1504.
55 C. R. Quijia, C. Lima, C. Silva, R. C. Alves, R. Frem and M. Chorilli, J Drug Deliv Sci Technol, 2021, 61, 102217.
56 P. Horcajada, R. Gref, T. Baati, P. K. Allan, G. Maurin, P. Couvreur, G. Férey, R. E. Morris and C. Serre, Chem Rev, 2012, 112, 1232–1268.
57 X. Li, L. Lachmanski, S. Safi, S. Sene, C. Serre, J. M. Grenèche, J. Zhang and R. Gref, Sci Rep, 2017, 7, 13142.
58 M.-L. Chen, S.-Y. Zhou, Z. Xu, L. Ding and Y.-H. Cheng, Molecules, 2019, 24, 3718.
59 I. Ahmed, J. Jeon, N. A. Khan and S. H. Jhung, Cryst Growth Des, 2012, 12, 5878–5881.
60 K. Oldham, Journal of Electroanalytical Chemistry, 1979, 105, 373–375.
61 P. Wang, H. Zhao, H. Sun, H. Yu, S. chen and X. Quan, RSC Adv., 2014, 4, 48912–48919.
62 I. Lavagnini, R. Antiochia and F. Magno, Electroanalysis, 2004, 16, 505–506.
63 S. Singh, A. Numan, Y. Zhan, V. Singh, A. Alam, T. Van Hung and N. D. Nam, RSC Adv, 2020, 10, 27288–27296.
64 S. Zhao, W. Yang and R. Y. Lai, Biosens Bioelectron, 2011, 26, 2442–2447.
65 M. Pourmadadi, J. S. Shayeh, S. Arjmand, M. Omidi and F. Fatemi, Microchemical Journal, 2020, 159, 105476.
66 F. Taati Yengejeh, J. Shabani Shayeh, M. Rahmandoust, F. Fatemi and S. Arjmand, J Biomed Mater Res B Appl Biomater, 2021, 109, 1505–1511.
67 R. Elshafey, P. Brisebois, H. Abdulkarim, R. Izquierdo, A. C. Tavares and M. Siaj, Electroanalysis, 2020, 32, 2205–2212.
68 M. Kim, R. Iezzi, B. S. Shim and D. C. Martin, Front Chem, DOI:10.3389/fchem.2019.00234.
69 S. Prabhulkar, S. Alwarappan, G. Liu and C.-Z. Li, Biosens Bioelectron, 2009, 24, 3524–3530.
70 S. Yarjoo, H. Siampour, M. Khalilipour, R. H. Sajedi, H. Bagheri and A. Moshaii, Sci Rep, 2024, 14, 10450.
71 S. Brunauer, P. H. Emmett and E. Teller, J Am Chem Soc, 1938, 60, 309–319.
72 E. P. Barrett, L. G. Joyner and P. P. Halenda, J Am Chem Soc, 1951, 73, 373–380.
73 B. LIPPENS, J Catal, 1965, 4, 319–323.
74 L. Gurvitsch." J. Phys. Chem. Soc. Russ, 1915, 47, 805-827.

Open Access Article. Published on 28 February 2025. Downloaded on 3/7/2025 11:32:11 AM.
This article is licensed under a Creative Commons Attribution-NonCommercial 3.0 Unported Licence.

Nanoscale Accepted Manuscript

View Article Online
DOI: 10.1039/D5NR00471C

Data availability

The data supporting this article have been included as part of the Supplementary Information

Open Access Article. Published on 28 February 2025. Downloaded on 3/7/2025 11:32:11 AM.
This article is licensed under a Creative Commons Attribution-NonCommercial 3.0 Unported Licence.

Nanoscale Accepted Manuscript